INTERNATIONAL JOURNAL FOR NUMERICAL METHODS IN FLUIDS
Int. J. Numer. Meth. Fluids 2008; **57**:555–581
Published online in Wiley InterScience (www.interscience.wiley.com). DOI: 10.1002/fld.1815

A partitioned coupling approach for dynamic fluid–structure interaction with applications to biological membranes

C. Wood*, †, A. J. Gil, O. Hassan and J. Bonet

Civil and Computational Engineering Centre, Swansea University, Swansea SA2 8PP, U.K.

SUMMARY

This paper presents a fully coupled three-dimensional solver for the analysis of time-dependent fluid–structure interaction. A partitioned time-marching algorithm is employed for the solution to the time-dependent coupled discretized problem, thus enabling the use of highly developed, robust and well-tested solvers for each field. Coupling of the fields is achieved through a conservative transfer of information at the fluid–structure interface. An implicit coupling is achieved when the solutions to the fluid and structure subproblems are cycled at each time step until convergence is reached. The three-dimensional unsteady incompressible fluid is solved using a powerful implicit dual time-stepping technique with an explicit multistage Runga–Kutta time stepping in pseudo-time and arbitrary Lagrangian–Eulerian formulation for the moving boundaries. A finite element dynamic analysis of the highly deformable structure is carried out with a numerical strategy combining the implicit Newmark time integration algorithm with a Newton–Raphson second-order optimization method. Various test cases are presented for benchmarking and to demonstrate the potential applications of this method. Copyright © 2008 John Wiley & Sons, Ltd.

Received 12 July 2007; Revised 28 February 2008; Accepted 28 February 2008

KEY WORDS: arbitrary Lagrangian–Eulerian; fluid–structure interaction; block Gauss–Seidel; partitioned schemes; nonlinear membrane analysis; artificial compressibility; dual time stepping

1. INTRODUCTION

The engineering modelling of multiphysics and multifield phenomena has over the past few decades stimulated enormous interest among scientists. In recent years, fluid–structure interaction (FSI) problems, in particular, have received increasing attention from the computational mechanics community. This has been made possible by the advances in the computational modelling of both fluid and solid structures and galvanized by further significant developments in terms of affordable

*Correspondence to: C. Wood, Civil and Computational Engineering Centre, Swansea University, Swansea SA2 8PP, U.K.
†E-mail: c.wood@swansea.ac.uk

Contract/grant sponsor: U.K. Engineering and Physical Sciences Research Council (EPSRC); contract/grant number: EP/D074258

computational resources. Within the current FSI research, time-dependent problems involving large structural deformations are of particular interest. Within the biomedical field, for example, the interaction of a viscous incompressible fluid, such as blood with a deformable membrane, as found within heart valves, arteries or veins represents an extraordinary challenge. Research within the biomedical field could influence many aspects of diagnosis and treatment as well as the design and implementation of components such as artificial heart valves, stents and many others [1–4].

Two categories of methods can be identified within FSI: non-boundary-fitting methods and boundary-fitting methods. The former category of non-boundary-fitting methods encompasses a range of closely related methods that originate from the immersed boundary method, pioneered by Peskin [5], whereas within the latter category of boundary-fitting methods, one of the most well-known techniques used is the arbitrary Lagrangian–Eulerian (ALE) formulation. Further distinctions between methods can be made depending on the choice of the time integration scheme employed; semi-discrete methods combining a discrete time integration scheme and spatial finite elements have been applied in [6–9], whereas finite element interpolations over both space and time domains, known as the space–time finite element method, have been applied in [10–14]. An important aspect of boundary-fitted methods, which makes them particularly advantageous within the modelling of the FSI problems, is the ability to capture the position of the moving fluid–structure interface very accurately.

In a general case, the ALE formulation allows arbitrary motion of points within a mesh with respect to their frame of reference by taking the convection of these points into account, as described in [15, 16] and many others. In the case of a FSI analysis, points within the reference spatial domain are moved in a Lagrangian manner to capture the moving interface between the fluid and the structure. Within the fluid domain, the Navier–Stokes equations are resolved with kinematic boundary conditions, which ensure the geometric conservation of the deforming fluid domain. The solid structure is usually analysed by a standard finite element technique resolved in a Lagrangian format [17, 18], together with natural boundary conditions provided by the Cauchy stress field generated at the interface with the fluid. Three further components are required to resolve the problem; firstly, a technique for transferring information at the interface, which guarantees the conservation of the system. Secondly, a non-expensive numerical strategy for the movement of the referential fluid mesh [19–21] and, finally, a robust and efficient solution procedure to ensure an accurate coupling of the system.

Two main techniques have emerged within the ALE methods for FSI: monolithic methods and partitioned methods. In the monolithic approach of [22], the discretized model equations for fluid and structure are integrated in time as one system for a simple piston problem, whereas in [11] the discretized model equations for fluid, structure and coupling conditions are formulated in a single equation system and solved simultaneously with the pseudo-structural moving mesh solved subsequently within the iteration loop. In contrast, by adopting a partitioned approach, each physical field is separately defined, discretized and numerically solved with coupling procedures applied to transfer the required interface information. Although the interacting fields are not solved simultaneously, a partitioned coupling scheme can require very few resolutions of the coupled problem at each time step for sufficient coupling to be achieved. These schemes are found to be very attractive as they allow the modularity of each of the field solvers to be retained [23], enabling the use of highly developed specialized codes that can be tailored to the specific problem at hand. The methodology presented in this paper can be included within this latter category.

The layout of this paper is outlined as follows: Section 2 presents the governing equations for the incompressible fluid field in an ALE format along with a finite volume solution algorithm.

DOI: 10.1002/fld

In Section 3, a finite element solution algorithm for the dynamic structural equilibrium equation is outlined. Section 4 presents a partitioned coupling procedure that enables the strong coupling of both fields. Furthermore, several strategies for the geometric deformation of the fluid domain are described. In Section 5, the robustness of the scheme is proven with a benchmark numerical example. Subsequently, to demonstrate the capabilities of the scheme, a fully three-dimensional biomedical model is presented. Finally, in Section 6 some conclusions are drawn.

2. UNSTEADY INCOMPRESSIBLE FLUID FLOW WITH MOVING BOUNDARIES

The transient incompressible flow field is governed by the Navier–Stokes continuity and momentum equations. To improve the conditioning of the resulting hyperbolic system of equations, the artificial compressibility approach, first proposed by Chorin [24] and later extended by Turkel [25], is employed. An implicit dual time-stepping technique with explicit multistage Runga–Kutta time stepping in pseudo-time and an ALE formulation enable unsteady flows with moving boundary components to be included.

2.1. Governing equations

With the development of an ALE solution procedure in mind, the time-dependent Navier–Stokes equations, modified using the artificial compressibility approach [24, 25], are considered in the integral form

$$\int_{\Omega(t)} \mathbf{P}^{-1}\frac{\partial \mathbf{U}}{\partial \tau}\,\mathrm{d}\Omega + \bar{\mathbf{I}}\frac{\mathrm{d}}{\mathrm{d}t}\int_{\Omega(t)} \mathbf{U}\,\mathrm{d}\Omega + \int_{\partial\Omega(t)} (\mathbf{F}_j - \bar{\mathbf{F}}_j) n_j\,\mathrm{d}S - \int_{\partial\Omega(t)} \mathbf{G}_j n_j\,\mathrm{d}S = \mathbf{0} \tag{1}$$

over a time-dependent three-dimensional domain $\Omega(t)$ bounded by a smooth closed surface $\partial\Omega(t)$. Here, n_j is the jth component of the outward unit normal vector to $\partial\Omega$ of a cartesian coordinate system, t is the physical time and τ denotes pseudo-time. The non-dimensionalized vectors of unknowns $\mathbf{U}$, the inviscid, ALE and viscous fluxes $\mathbf{F}_j$, $\bar{\mathbf{F}}_j$ and $\mathbf{G}_j$ are given by

$$\mathbf{U} = \begin{bmatrix} p \\ u_1 \\ u_2 \\ u_3 \end{bmatrix}, \quad \mathbf{F}_j = \begin{bmatrix} u_j \\ u_1 u_j + p\delta_{1j} \\ u_2 u_j + p\delta_{2j} \\ u_3 u_j + p\delta_{3j} \end{bmatrix}, \quad \bar{\mathbf{F}}_j = \begin{bmatrix} 0 \\ u_1 \hat{u}_j \\ u_2 \hat{u}_j \\ u_3 \hat{u}_j \end{bmatrix}, \quad \mathbf{G}_j = \begin{bmatrix} 0 \\ \tau_{1j} \\ \tau_{2j} \\ \tau_{3j} \end{bmatrix} \tag{2}$$

where the standard summation convention on repeated indices is used and $j = 1, 2, 3$. In these expressions, ρ_{F} denotes the fluid density, u_j the component of the velocity vector in the x_j direction, p the pressure, $\hat{u}_j$ the velocity of the control-volume boundary and δ_{ij} the Kronecker delta operator. Additionally, τ_{ij} are the components of the deviatoric stress tensor formulated as

$$\tau_{ij} = \frac{1}{Re}\left(\frac{\partial u_i}{\partial x_j} + \frac{\partial u_j}{\partial x_i}\right) \tag{3}$$

DOI: 10.1002/fld

Finally, $\bar{\mathbf{I}}$ is a modified unit matrix and $\mathbf{P}$ is a preconditioning matrix for the pseudo-time equation system [24, 25]

$$\bar{\mathbf{I}}=\begin{bmatrix}0&0&0&0\\0&1&0&0\\0&0&1&0\\0&0&0&1\end{bmatrix},\quad \mathbf{P}=\begin{bmatrix}\beta^2&0&0&0\\0&1&0&0\\0&0&1&0\\0&0&0&1\end{bmatrix} \tag{4}$$

where the parameter β can be viewed as a relaxation parameter for the pseudo-time solution procedure, with its value selected so as to optimize the convergence of the solution procedure [26]. On the basis of numerical experiments, the value of β is defined as

$$\beta^2=\max(\beta^2_{\min}, C_\beta|\mathbf{u}|^2) \tag{5}$$

with $\beta^2_{\min}=1$ and $C_\beta=2.5$.

2.2. Physical time discretization

Following the discretization of the physical time t, Equation (1) may be expressed as

$$[\mathbf{P}^m]^{-1}\int_{\Omega(t)}\frac{\mathrm{d}\mathbf{U}}{\mathrm{d}\tau}\bigg|^m \mathrm{d}\Omega+\bar{\mathbf{I}}\frac{\mathrm{d}}{\mathrm{d}t}\int_{\Omega(t)}\mathbf{U}|^m\,\mathrm{d}\Omega+\int_{\partial\Omega(t)}(\mathbf{F}^m_j-\bar{\mathbf{F}}^m_j-\mathbf{G}^m_j)n_j\,\mathrm{d}S=\mathbf{0} \tag{6}$$

where the superscript m denotes an evaluation at time $t=t^m$. The three-level, second-order, backward difference representation for a control volume $\Omega_I(t)$

$$\frac{\mathrm{d}}{\mathrm{d}t}\int_{\Omega_I(t)}\mathbf{U}|^m\,\mathrm{d}\Omega=\frac{1}{\Delta t}\left(\frac{3}{2}\Omega^m_I\mathbf{U}^m-2\Omega^{m-1}_I\mathbf{U}^{m-1}+\frac{1}{2}\Omega^{m-2}_I\mathbf{U}^{m-2}\right)=\mathscr{T}(\mathbf{U}^m) \tag{7}$$

is employed for the approximation of the physical time derivative, where $\Delta t=t^{m+1}-t^m$ denotes the physical time step.

2.3. Dual mesh construction

To develop a cell vertex finite volume method for the spatial discretization of the governing equations, identification of a dual mesh is required. This dual mesh, illustrated in Figure 1, is constructed by connecting edge midpoints, element centroids and face centroids of the basic tetrahedral fluid mesh, in such a manner that only one node is contained within each dual mesh cell. The dual mesh cells then form the control volumes for the subsequent finite volume algorithm. Equation (6) is then applied to each dual mesh volume in turn. For the sake of brevity, here we develop only the form of the discrete equation at interior nodes I of the mesh. For a more detailed presentation of the algorithm, refer [27–30].

DOI: 10.1002/fld

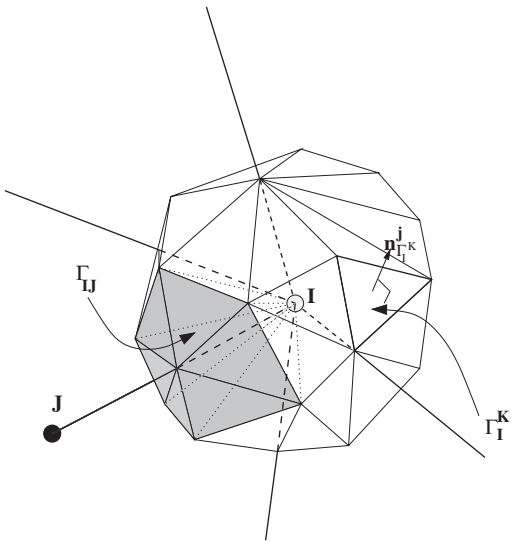

Figure 1. The dual mesh surrounding an internal node I.

2.4. Treatment of the inviscid and viscous fluxes

To evaluate the approximation of the integral, we adopt an edge-based implementation in which the coefficients for each edge are calculated by using the dual mesh segment associated with the edge. For an internal edge connecting nodes I and J, these coefficients are computed as

$$\mathscr{C}_{j,IJ}^m = \sum_{K \in \Gamma_{IJ}} A_{\Gamma_I^K}^m n_j^{\Gamma_I^K,m} \tag{8}$$

where $A_{\Gamma_I^K}^m$ is the area of facet Γ_I^K, and $n_j^{\Gamma_I^K,m}$ is the jth component of the unit normal vector to the facet from the viewpoint of node I at time level m. Then, assuming that the integrand is constant over the segment and equal to its value at the midpoint of the edge, the inviscid and viscous flux terms are approximated as

$$\int_{\partial\Omega_I^m} (\mathbf{F}_j^m - \mathbf{G}_j^m) n_j \, \mathrm{d}S = \sum_{J \in \Lambda_I} \frac{\mathscr{C}_{j,IJ}^m}{2} [(\mathbf{F}_{j,I}^m + \mathbf{F}_{j,J}^m) - (\mathbf{G}_{j,I}^m + \mathbf{G}_{j,J}^m)] \tag{9}$$

where Λ_I denotes the set of all nodes connected to node I by edges in the mesh. From Equations (2) and (3), it is apparent that the evaluation of $\mathbf{G}_{j,I}^m$ and $\mathbf{G}_{j,J}^m$ requires the evaluation of the gradients. At a typical interior node I, these derivatives are obtained, by again using the approach adopted above, as

$$\left.\frac{\partial u_i}{\partial x_j}\right|^I = \frac{1}{\Omega_I} \sum_{J \in \Lambda_I} \frac{\mathscr{C}_{j,IJ}}{2} (u_{i,I} + u_{i,J}) \tag{10}$$

which results in a second-order accurate discretization with a non-compact computational stencil which stretches over five points.

DOI: 10.1002/fld

2.5. Treatment of the ALE fluxes

An important property of Equation (1) is geometric conservation. The geometric conservation law (GCL), first shown in [31], requires that the control-volume movement itself has no direct effect on the fluxes, in the sense that if the unknown field is constant, the numerical solution does not change in time in the presence of a moving mesh, i.e. from Equation (1)

$$\frac{\mathrm{d}}{\mathrm{d}t}\int_{\Omega(t)} \mathrm{d}\Omega - \int_{\partial\Omega(t)} \hat{u}_j\, n_j\, \mathrm{d}S = 0 \tag{11}$$

It is desirable to retain this quality numerically, after discretization. This has led to the so-called discrete geometric conservation law (DGCL), as advocated in [32–34], which governs the geometric parameters of the numerical scheme, such as grid positions and velocities, so that the corresponding numerical scheme exactly reproduces a constant solution.

The numerical integration of the ALE fluxes is performed in the usual manner by summing the edge contribution with the ALE edge coefficient $\mathscr{D}_{IJ}^m$ introduced such that

$$\int_{\partial\Omega_I^m} \bar{\mathbf{F}}_j^m n_j\, \mathrm{d}S = \sum_{J\in\Lambda_I} \frac{\mathscr{D}_{IJ}^m}{2}(\bar{\mathbf{U}}_I^m + \bar{\mathbf{U}}_J^m) \tag{12}$$

where $\bar{\mathbf{U}} = [0, u_1, u_2, u_3]^{\mathrm{T}}$. The task of finding ALE coefficients that render the scheme geometrically conservative is not trivial and has been treated by a number of authors [31–35]. Here the approach of [35] is followed. From Equation (11), it can be stated that to maintain geometric conservation at a discrete level, the change in volume of a moving cell I must be equal to the volume swept by the its boundaries from time t^m to t^{m+1}

$$\Omega_I^{m+1} - \Omega_I^m = \int_{t^m}^{t^{m+1}} \int_{\partial\Omega_I(t)} \hat{u}_i\, n_i\, \mathrm{d}\Omega\, \mathrm{d}t \tag{13}$$

Assuming that the mesh moves in a linear manner between time levels t^m and t^{m+1}, as illustrated in Figure 2, a local GCL expressing the change in volume due to the movement of a triangular facet Γ_I^K between time levels t^m and t^{m+1} can be expressed as

$$\delta V_{\Gamma_I^K}^{m+1,m} = \Delta t\, \hat{u}_i^{\Gamma_I^K,*} n_i^{\Gamma_I^K,*} A_{\Gamma_I^K}^* \tag{14}$$

where $\hat{u}_i^{\Gamma_I^K,*}$ is the average facet velocity, $A_{\Gamma_I^K}^*$ is the average facet area and $n_i^{\Gamma_I^K,*}$ is the average normal. This term can be recognized as the contribution to the numerical ALE coefficient of a single facet multiplied by the time step. Summing over all the facets of the boundary surface of the control volume connected to the edge IJ yields the expression for the edge-based ALE coefficient for a first-order discretization in time as

$$\mathscr{D}_{IJ}^{m+1} = \frac{1}{\Delta t} \sum_{K\in\Gamma_{IJ}} \delta V_{\Gamma_I^K}^{m+1,m} \tag{15}$$

If the second-order time discretization given in Equation (7) is applied, a modified version of the ALE flux must be employed to ensure discrete geometric conservation. The modification

$$\hat{\mathscr{D}}_{IJ}^{m+1} = \tfrac{3}{2}\mathscr{D}_{IJ}^{m+1} - \tfrac{1}{2}\mathscr{D}_{IJ}^m$$

DOI: 10.1002/fld

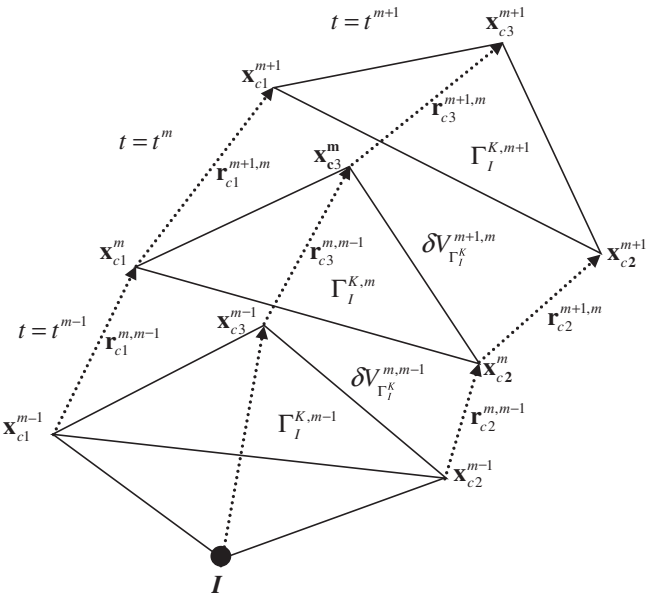

Figure 2. The linear motion of a triangular facet of the dual mesh over time levels $m-1$, m and $m+1$.

is adopted [36], which makes the numerical ALE coefficient second order in time. In addition, velocity boundary conditions at the moving boundary are applied as

$$\mathbf{u}_I^{w,m+1} = \frac{1}{\Delta t}(\mathbf{x}_I^{m+1} - \mathbf{x}_I^m) \tag{16}$$

if a first order in time scheme is used or

$$\mathbf{u}_I^{w,m+1} = \frac{1}{\Delta t}\left(\frac{3}{2}\mathbf{x}_I^{m+1} - 2\mathbf{x}_I^m + \frac{1}{2}\mathbf{x}_I^{m-1}\right) \tag{17}$$

if a second-order backwards difference in time scheme is used, which is consistent with the dual mesh velocity definition.

2.6. Solution procedure

If $\mathscr{S}_{j,IJ}$ $(j=1,2,3)$ denotes the components of a unit vector in the direction of the vector $\mathscr{C}_{j,IJ}$, Equation (6) may be re-expressed as

$$\Omega_I \frac{\mathrm{d}\mathbf{U}_I^m}{\mathrm{d}\tau} = \mathscr{R}_I^m \tag{18}$$

where

$$\mathscr{R}_I^m = \bar{\mathbf{I}}\mathscr{T}(\mathbf{U}_I^m) - \mathbf{P}_I^m \sum_{J\in\Lambda_I}\left\{\frac{\mathscr{C}_{IJ}^m}{2}[(\mathscr{F}_I^m + \mathscr{F}_J^m) - (\mathscr{G}_I^m + \mathscr{G}_J^m)] - \frac{\mathscr{D}_{IJ}^m}{2}(\bar{\mathbf{U}}_I^m + \bar{\mathbf{U}}_J^m)\right\} \tag{19}$$

DOI: 10.1002/fld

and

$$\mathscr{F}_I = \mathscr{S}_{j,IJ}\mathbf{F}_{j,I}, \quad \mathscr{G}_I = \mathscr{S}_{j,IJ}\mathbf{G}_{j,I}, \quad \mathscr{C}_{IJ} = (\mathscr{C}_{j,IJ}\mathscr{C}_{j,IJ})^{1/2} \tag{20}$$

At each physical time level $t = t_m$, the value of $\mathbf{U}^m$ is obtained by integrating Equation (18) in pseudo-time to steady state using an explicit three-stage Runga–Kutta scheme. A stable computational procedure is achieved by the explicit of an artificial viscosity term, constructed in the Jameson–Schmidt–Turkel manner [37]. Parallelization of the solution algorithm is implemented by the domain decomposition multigrid approach using the single program multiple data parallel architecture with the message passing interface model for communication of data. A more detailed description of the solution procedure as well as verification of the robustness of the algorithm may be found in References [27–30].

3. FINITE STRAIN HYPERELASTIC STRUCTURAL DYNAMICS

3.1. Kinematics and kinetics

From a kinetic perspective, the principle of conservation of linear momentum must be fulfilled. This may be expressed in spatial terms as

$$\rho_S(\ddot{\mathbf{x}} - \mathbf{f}) - \nabla \cdot \boldsymbol{\sigma} = \mathbf{0} \tag{21}$$

where ρ_S is the density of the deforming solid, vector $\ddot{\mathbf{x}}$ represents the acceleration and body forces are given by $\mathbf{f}$. The symmetric second-order tensor $\boldsymbol{\sigma}$ denotes the Cauchy stress tensor. The dynamic equilibrium equation is integrated over a solid volume v with boundary ∂v along a virtual velocity field $\delta\mathbf{v}$ to yield the virtual work expression of the dynamic equilibrium equation as follows:

$$\delta W(\phi, \delta\mathbf{v}) = \int_v \boldsymbol{\sigma} : \delta\mathbf{d}\, \mathrm{d}v - \int_v \mathbf{f} \cdot \delta\mathbf{v}\, \mathrm{d}v - \int_{\partial v} \mathbf{t} \cdot \delta\mathbf{v}\, \mathrm{d}a + \int_v \rho_S \ddot{\mathbf{x}} \cdot \delta\mathbf{v}\, \mathrm{d}v = 0 \tag{22}$$

where $\mathbf{t}$ is the traction vector acting on the boundary, which results from considering Gauss' theorem, and $\delta\mathbf{d}$ represents the rate of deformation tensor of the virtual velocity field. This expression is highly nonlinear due to both geometric and material effects.

Owing to the large deformation nature of the solid displacement field, a finite strain continuum approach is required to describe the solid behaviour. The solid structure is described in a standard Lagrangian format such that the current position $\mathbf{x}$ of a material particle is related to the initial position $\mathbf{X}$ by mapping ϕ and the gradient of this mapping gives the deformation gradient tensor $\mathbf{F}$

$$\mathbf{x} = \phi(\mathbf{X}), \quad \mathbf{F} = \frac{\partial \phi}{\partial \mathbf{X}} \tag{23}$$

The symmetric right Cauchy–Green strain tensor $\mathbf{C}$ and the Lagrangian strain tensor $\mathbf{E}$, which measure the deformation that has taken place between the initial and final configurations, can be obtained as

$$\mathbf{E} = \tfrac{1}{2}(\mathbf{C} - \mathbf{I}), \quad \mathbf{C} = \mathbf{F}^{\mathrm{T}}\mathbf{F} \quad \text{and} \quad J = \det(\mathbf{F}) \tag{24}$$

where the Jacobian J expresses the volume change between the initial and final configurations.

DOI: 10.1002/fld

3.2. Large strain hyperelasticity

The formulation presented in this paper encompasses large strain hyperelasticity in principal directions and is based on the stored strain-energy functional Ψ. The strain-energy functional for hyperelastic materials may be formulated as functions of the strain invariants. Therefore, for the isotropic case, Ψ is a function of the three principal invariants of the right Cauchy–Green tensor $\mathbf{C}$ as

$$\Psi(\mathbf{C}) = \Psi(\mathrm{I}_C, \mathrm{II}_C, \mathrm{III}_C) \tag{25}$$

where the strain invariants are found by

$$I_C = \mathrm{tr}\,\mathbf{C}, \quad \mathrm{II}_C = \mathbf{C}:\mathbf{C}, \quad \mathrm{III}_C = \det\mathbf{C} = J^2 \tag{26}$$

Equivalently, Ψ can be formulated in the alternative form

$$\Psi(\mathbf{C}) = \Psi(\lambda_1^2, \lambda_2^2, \lambda_3^2) \tag{27}$$

where $\{\lambda_A\}_{A=1,2,3}$ are the three real, positive eigenvalues of the eigenvalue problem $(\mathbf{C}-\lambda_A^2\mathbf{I})\mathbf{e}_A = \mathbf{0}$ and correspond to the three eigenvectors $\{\mathbf{e}\}_{A=1,2,3}$, the principal directions of strains. The three values $\{\lambda_{A=1,2,3}\}$ are the so-called principal stretches and $\mathbf{I}$ denotes the identity tensor. The strain invariants of Equation (25) can be expressed as functions of λ_A^2 as

$$\mathrm{I}_C = \lambda_1^2+\lambda_2^2+\lambda_3^2, \quad \mathrm{II}_C = \lambda_1^2\lambda_2^2+\lambda_1^2\lambda_3^2+\lambda_2^2\lambda_3^2, \quad \mathrm{III}_C = \lambda_1^2\lambda_2^2\lambda_3^2 \tag{28}$$

The stress–deformation relationship for a hyperelastic material is generated from the continuous strain-energy function Ψ by the relationship

$$\mathbf{S} = \frac{\partial\Psi}{\partial\mathbf{E}} = 2\frac{\partial\Psi}{\partial\mathbf{C}} \tag{29}$$

where $\mathbf{S}$ denotes the second Piola–Kirchoff stress tensor, work conjugate to $\mathbf{E}$.

The Neo–Hookean material model is the simplest case of a hyperelastic potential, which in the case of incompressibility yields an expression for Ψ as

$$\Psi(\mathbf{C}) = \mu\,\mathrm{tr}[\mathbf{E}] = \tfrac{1}{2}\mu(\mathrm{tr}[\mathbf{C}]-3) \tag{30}$$

where μ symbolizes the material Lamè coefficient. Incompressible materials have the well-known property that the volume is preserved, leading to the condition that

$$J = \frac{\mathrm{d}v}{\mathrm{d}V} = \mathrm{III}_C^{1/2} = \det\mathbf{C}^{1/2} \equiv 1 \tag{31}$$

where the dilational ratio J expresses the ratio of the deformed volume $\mathrm{d}v$ of a body to its corresponding undeformed volume $\mathrm{d}V$. This incompressibility, using Equation (28), may be expressed in terms of the principal stretches as

$$\lambda_1\lambda_2\lambda_3 = 1 \tag{32}$$

In the particular case of plane stress, the incompressibility condition implies that $C_{33}\mathrm{III}_{C_{2\times2}} = 1$, where $\mathrm{III}_{C_{2\times2}}$ is the determinant of the in-plane components of $\mathbf{C}$. Substituting C_{33} into Equation (30) gives the hyperelastic potential and the resulting second Piola–Kirchoff stress tensor for an incompressible Neo–Hookean type of material in the plane stress case as

$$\Psi(\mathbf{C}) = \tfrac{1}{2}\mu(\mathrm{I}_C + \mathrm{III}_C^{-1} - 3), \quad \mathbf{S} = \mu(\mathbf{I} - \mathrm{III}_C^{-1}\mathbf{C}^{-1}) \tag{33}$$

DOI: 10.1002/fld

Within the field of biomedicine, membranes subjected to low pressures tend to behave similar to rubber-like materials [38] and a Neo–Hookean or Mooney–Rivlin hyperelastic potential is often used. In this study, membranes are modelled using a Neo–Hookean-type material frequently encountered in the literature [18], with a hyperelastic potential defined in terms of the logarithmic stretches and the two-material Lamè parameters, with no bending resistance.

Considering the plane stress case corresponding to a membrane analysis, stress in the third direction is constrained, i.e. $\sigma_{33}=0$. The hyperelastic potential Ψ is expressed in terms of the membrane principal stretches λ_1 and λ_2 as

$$\Psi(\lambda_1,\lambda_2)=\mu[(\ln\lambda_1)^2+(\ln\lambda_2)^2]+\frac{\bar{\lambda}}{2}(\ln j)^2 \tag{34}$$

where the parameter α and the effective Lamè coefficient $\bar{\lambda}$ are given by

$$\alpha=\frac{2\mu}{\lambda+2\mu},\quad \bar{\lambda}=\alpha\lambda \tag{35}$$

and the three-dimensional volume ratio J is found as a function of the planar component j as $J=j^{\alpha}$. The incompressibility constraint is enforced exactly by adjusting the eigenvalue of the tensor $\mathbf{C}$ corresponding to the principal direction normal to the tangent plane of the membrane. Thus, the principal stretch normal to the membrane surface, λ_3, simplifies to a dependent value, namely the inverse of the determinant of the in-plane components of $\mathbf{C}$, so that the current membrane thickness h is always determined by the relationship

$$\lambda_3=\frac{1}{\lambda_1\lambda_2}=\frac{h}{H} \tag{36}$$

where H is the initial membrane thickness. The solution to other three-dimensional problems with incompressible materials employs near-incompressibility to enforce the incompressibility condition, thereby a volumetric energy component containing a penalty term is added to the distortional component of the strain-energy functional [18].

3.3. Linearized equilibrium equations

The solution to the virtual work representation of the dynamic equilibrium equations given in Equation (22) is found at discrete time intervals for the given material and loading conditions by determining a deformed configuration ϕ, which is in a state of dynamic equilibrium. This equilibrium configuration is found using a Newmark time integration scheme in conjunction with a Newton–Raphson iterative solution procedure and therefore requires a linearized form of the nonlinear dynamic equilibrium equations.

Considering the implicit Newmark time integration scheme, the algorithm relating the approximations to the displacement, velocity and acceleration at time step m, denoted by $\mathbf{x}_m$, $\dot{\mathbf{x}}_m$ and $\ddot{\mathbf{x}}_m$, respectively, can be stated in its general form as

$$\begin{aligned}\mathbf{x}_{m+1}&=\mathbf{x}_m+\Delta t\dot{\mathbf{x}}_m+\Delta t^2[(\tfrac{1}{2}-\beta)\ddot{\mathbf{x}}_m+\beta\ddot{\mathbf{x}}_{m+1}]\\ \dot{\mathbf{x}}_{m+1}&=\dot{\mathbf{x}}_m+\Delta t[(1-\gamma)\ddot{\mathbf{x}}_m+\gamma\ddot{\mathbf{x}}_{m+1}]\end{aligned} \tag{37}$$

for time $t=m\Delta t$, where Δt is the time step. The selection of parameters $\gamma=0.5$ and $\beta=0.25$ corresponds to the trapezoidal rule. This scheme is unconditionally stable and second-order accurate

DOI: 10.1002/fld

for linear analysis, and when used with the appropriate time step size and sufficient equilibrium iteration convergence, it is ideal for the solution to this nonlinear dynamic problem [39]. The kinematic relationships in Equation (37) along with the virtual work expression in Equation (22) form a system of nonlinear equations that are solved according to a predictor–corrector scheme. Once a predicted value is established, namely $\mathbf{x}_{m+1}^k$, $\dot{\mathbf{x}}_{m+1}^k$ and $\ddot{\mathbf{x}}_{m+1}^k$, correction is carried out upon linearization along an incremental direction set by $\Delta\mathbf{x}$, $\Delta\dot{\mathbf{x}}$ and $\Delta\ddot{\mathbf{x}}$, respectively. Importantly, the Newmark algorithm enables the increment in displacement $\Delta\mathbf{x}$ or velocity $\Delta\dot{\mathbf{x}}$ to be expressed in terms of the increment in acceleration $\Delta\ddot{\mathbf{x}}$ as follows:

$$\Delta\mathbf{x} = \beta\Delta t^2\Delta\ddot{\mathbf{x}}, \quad \Delta\dot{\mathbf{x}} = \gamma\Delta t\Delta\ddot{\mathbf{x}} \tag{38}$$

Given the highly nonlinear nature of Equation (22), a consistent linearization procedure is required for optimum convergence. For a trial solution ϕ_k, the terms of the above spatial virtual work equation can be linearized in the direction of an increment in the acceleration as follows:

$$\delta W(\phi_k, \delta\mathbf{v}) + D\delta W(\phi_k, \delta\mathbf{v})[\Delta\ddot{\mathbf{x}}] = 0 \tag{39}$$

where the directional derivative term represents the virtual work δW done during the increment in acceleration from $\ddot{\mathbf{x}}$ to $(\ddot{\mathbf{x}}+\Delta\ddot{\mathbf{x}})$. The directional derivative of $\delta W(\phi, \delta\mathbf{v})$ in the direction of an increment in acceleration $\Delta\ddot{\mathbf{x}}$ can be considered in terms of the internal, external and inertial virtual work components as

$$D\delta W(\phi, \delta\mathbf{v})[\Delta\ddot{\mathbf{x}}] = D\delta W_{\text{int}}(\phi, \delta\mathbf{v})[\Delta\ddot{\mathbf{x}}] - D\delta W_{\text{ext}}(\phi, \delta\mathbf{v})[\Delta\ddot{\mathbf{x}}] + D\delta W_{\text{ine}}(\phi, \delta\mathbf{v})[\Delta\ddot{\mathbf{x}}] \tag{40}$$

Discretization of the linearized internal and external virtual work terms yields internal and external tangent stiffness matrix components, derived from constitutive, initial stress and external forces, whereas the discretized linearized inertia virtual work term yields the consistent mass matrix.

3.4. Finite element discretization

The spatial discretization of the continuous surface or volume is performed using an assembly of isoparametric displacement-based finite elements, as described in standard texts such as [18, 39, 40], with a library of elements ranging from 3-noded triangular surface elements with linear shape functions (or equivalent 9-noded volume elements) to 16-noded quadrilateral surface elements with cubic shape functions (or equivalent 64-noded volume elements), depending upon the problem under consideration.

The finite element discretization of the equations of equilibrium yields the vectors of internal, external and inertia nodal equivalent forces at node a of a finite element (e), namely $\mathbf{T}_a^{(e)}$, $\mathbf{F}_a^{(e)}$ and $\mathbf{I}_a^{(e)}$ as

$$\mathbf{T}_a^{(e)} = \int_{v^{(e)}} \boldsymbol{\sigma}\nabla N_a \, \mathrm{d}v, \quad \mathbf{F}_a^{(e)} = \int_{v^{(e)}} N_a\mathbf{f}\,\mathrm{d}v + \int_{\partial v^{(e)}} N_a\mathbf{t}\,\mathrm{d}a, \quad \mathbf{I}_a^{(e)} = \int_{v^{(e)}} \rho_{\mathrm{S}} N_a\ddot{\mathbf{x}}\,\mathrm{d}v \tag{41}$$

where N_a is the shape function corresponding to node a. Summing over all the nodes N of the finite element discretization, the total virtual work $\delta W(\phi, \delta\mathbf{v})$ is given by

$$\delta W(\phi, \delta\mathbf{v}) = \sum_{a=1}^{N} \delta W(\phi, N_a\delta\mathbf{v}) = \sum_{a=1}^{N} \delta\mathbf{v}_a \cdot (\mathbf{T}_a - \mathbf{F}_a + \mathbf{I}_a) = 0 \tag{42}$$

DOI: 10.1002/fld

Assembling the nodal equivalent forces into global arrays and noting that the virtual nodal velocities $\delta\mathbf{v}_a$ are arbitrary, the complete set of discretized nonlinear equilibrium equations can be expressed symbolically in terms of the residual force $\mathbf{R}$ as

$$\mathbf{R}(\mathbf{x}) = \mathbf{T}(\mathbf{x}) - \mathbf{F}(\mathbf{x}) + \mathbf{I}(\ddot{\mathbf{x}}) = \mathbf{0} \tag{43}$$

3.5. Solution procedure

A Newmark predictor–corrector algorithm given in Equation (37) is employed for dynamic computational simulations and can be straightforwardly reduced to the static analysis case when necessary. Following the finite element spatial discretization described previously, the discretized nonlinear dynamic equations can be presented as

$$\mathbf{R} = \mathbf{M}\ddot{\mathbf{x}}_{m+1} + \mathbf{C}\dot{\mathbf{x}}_{m+1} + \mathbf{T}(\mathbf{x}_{m+1}) - \mathbf{F}(\mathbf{x}_{m+1}) = \mathbf{0} \tag{44}$$

where $\mathbf{M}$ represents the assembled mass matrix, $\mathbf{C}$ a possible damping matrix to be included within the calculations, $\mathbf{T}$ the assembled vector of equivalent internal forces, $\mathbf{F}$ the assembled vector of equivalent external forces and $\mathbf{R}$ the assembled out of balance or residual equivalent force vector. A quadratically convergent Newton–Raphson iterative algorithm is employed for the resolution of the above system of equations (44) as follows:

$$\ddot{\mathbf{x}}_{m+1}^{k+1} = \ddot{\mathbf{x}}_{m+1}^{k} + \Delta\ddot{\mathbf{x}}^{k}, \quad \Delta\ddot{\mathbf{x}}^{k} = -\left[\left.\frac{\partial \mathbf{R}}{\partial \ddot{\mathbf{x}}}\right|_{\ddot{\mathbf{x}}=\ddot{\mathbf{x}}_{m+1}^{k}}\right]^{-1} \mathbf{R}_{m+1}^{k} \tag{45}$$

where

$$\left.\frac{\partial \mathbf{R}}{\partial \ddot{\mathbf{x}}}\right|_{\ddot{\mathbf{x}}=\ddot{\mathbf{x}}_{m+1}^{k}} = \mathbf{M} + \gamma\Delta t\mathbf{C} + \beta\Delta t^2(\mathbf{K}^{\text{int}} - \mathbf{K}^{\text{ext}}) \tag{46}$$

and the convergence of the scheme is improved by the use of a parametric line search procedure.

4. PARTITIONED SOLUTION PROCEDURE

4.1. Partitioned fluid–structure interface coupling

Following the approach of Farhat *et al.* [32], a conventional serial staggered solution procedure with full subiteration at each time level, shown schematically in Figure 3, is applied. The four steps of the scheme are outlined as follows:

1. Predict/correct the motion of the 'wet' boundary of the structure and update the deforming fluid mesh.
2. Compute the new fluid pressure and velocity fields $\mathbf{U}_m^{\text{F}}$ for the updated deforming fluid mesh and the corresponding mesh velocities $\hat{\mathbf{u}}_{m-1}$, which enforce the displacement and velocity boundary conditions of the moving fluid–structure interface.
3. Transfer the new fluid pressure field $\mathbf{p}_m^{\text{F}}$ to the structural discretization and calculate the updated structural loading.
4. Compute the new dynamic structural response $\mathbf{U}_m^{\text{S}}$ to the fluid-induced loading.

DOI: 10.1002/fld

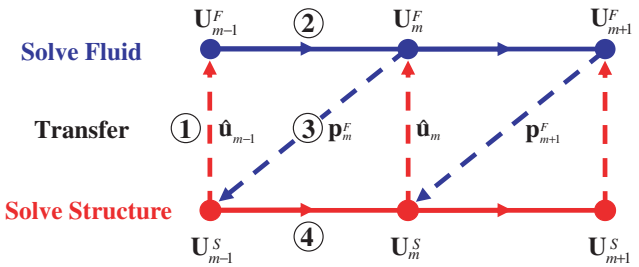

Figure 3. Partitioned staggered solution procedure with full subiteration.

Such a block Gauss–Seidel iterative scheme provides strong coupling of the partitioned fluid and structure subproblems and, when implemented in conjunction with the implicit dual time-stepping the scheme of the fluid solver and implicit Newmark/Newton–Raphson scheme of the structural solver, enables a large physical time step to be maintained. Depending upon the time step selected and/or the combined physical and geometrical parameters of the problem—certain classes of problem frequently encountered in biomedical modelling can be severely destabilized by the effects of the so-called added-mass phenomena [41, 42]—subiterations may or may not be required at each time level for strong coupling to be achieved. In the examples presented here, matching discretizations have been generated at the interface to avoid the errors associated with data interpolation on highly non-matching discretizations during this implementation stage. Kinetic energy is exchanged at the fluid–structure interface through a Dirichlet–Neumann partitioning as follows: The dynamic mesh algorithm applies the Dirichlet boundary conditions defined by the structural solution at the interface. The vector of unknowns of the fluid domain $\mathbf{U}_m^{\mathrm{F}}$ is solved at time m for this deformed mesh, with mesh velocities $\hat{\mathbf{u}}_{m-1}$ calculated in a manner that is consistent with the discrete time integration scheme of the fluid solver. The vector of unknowns of the structure domain $\mathbf{U}_m^{\mathrm{S}}$ is then solved at time m for the Neumann boundary conditions given by the fluid loading at the interface. These Neumann boundary conditions are composed of normal pressures and tangential shear forces due to the viscous fluid in contact with the structure. However, in order to simplify this transfer of forces, it is considered that at this stage the transferred loadings will be composed solely of the fluid pressure component $\mathbf{p}_m^{\mathrm{F}}$, which is taken as an average of the nodal values for that surface element. Although this simplification could clearly lead to misleading results in cases where shear effects are significant, care will be taken to select examples in which any potential shear loading effect is negligible.

For strong coupling of the interacting fields, it is necessary that both displacement boundary conditions and velocity boundary conditions are satisfied at the interface. That is,

$$\mathbf{x}_m^{\mathrm{S}} = \mathbf{x}_m^{\mathrm{F}}, \quad \dot{\mathbf{x}}_m^{\mathrm{S}} = \dot{\mathbf{x}}_m^{\mathrm{F}} \tag{47}$$

where $\mathbf{x}_m^{\mathrm{S}}$ and $\mathbf{x}_m^{\mathrm{F}}$ and $\dot{\mathbf{x}}_m^{\mathrm{S}}$ and $\dot{\mathbf{x}}_m^{\mathrm{F}}$ are the position and velocity, respectively, of the interface in the fluid and structural domains at time m. The partitioned solution scheme ensures that the compatibility of the fluid and structural domain displacement fields is maintained at the interface all times, by applying the structural displacements at the interface as Dirichlet boundary conditions for the dynamic mesh algorithm. Compatibility of the fluid and structural domain velocity fields at the interface is achieved at each time step through corrective subiterations over the fluid and structure subproblems.

DOI: 10.1002/fld

The relative convergence of the overall coupling procedure is measured at each time step as an L^2 norm of the variation in pressure at the interface surface over successive subiterations relative to the pressure at the first subiteration. The L^2 norm of the variation in pressure at subiteration n, denoted by $\|\Delta p^n\|_2$, and the reference pressure norm, denoted by $\|\Delta p^0\|_2$, where $n=0$ indicates the first subiteration, are calculated by

$$\|\Delta p^n\|_2=\sqrt{\sum_{i=1}^{\text{nnodes}}(p_i^n-p_i^{n-1})^2},\quad \|\Delta p^0\|_2=\sqrt{\sum_{i=1}^{\text{nnodes}}(p_i^0)^2} \tag{48}$$

The relative convergence of the interface pressure per time step is then expressed as 1×10^N, where order N is given by

$$N=\log\|\Delta p^n\|_2-\log\|\Delta p^0\|_2 \tag{49}$$

4.2. Dynamic grid deformation

The application of the moving interface boundary conditions in time requires that the position of the interface is captured accurately within the fluid domain mesh, ideally while maintaining the connectivity of the original mesh and the required mesh quality. The spring analogy, first developed by Batina [19] and later improved by Degand and Farhat [20], is a straightforward iterative strategy that is widely used in aerodynamics and unsteady flow solutions. Every element edge within the mesh is treated as a spring, with stiffness usually taken as the inverse of the length of that edge. The static equilibrium equations for this network of springs are then solved for small increments in the deforming boundary, by solving for the system

$$\sum_{J\in\Lambda_I} s_{IJ}(l_{IJ}-l_{IJ}^{\text{prev}})=0 \tag{50}$$

where l_{IJ}^{prev} and l_{IJ} are the lengths of the edge between nodes I and J before and after the movement, respectively, and s_{IJ} is the spring coefficient. This approach is robust for moderate boundary movements but may not be sufficient for cases with complex movement patterns.

An alternative method to apply dynamic grid deformation, which is also implemented in this study, is based on a Delaunay graph mapping [21]. This is achieved in the following manner: First, using a Delaunay triangulation [43], the boundary discretization is generated. An example of the boundary-conforming Delaunay triangulation of interior and exterior boundary points is shown in Figure 4(a). All of the Delaunay triangulation points are coincident with the boundary points of the unstructured discretization used for the fluid computation, shown in Figure 4(b), and therefore the Delaunay triangulation forms the reference graph of the moving grid problem.

The Delaunay graph mapping procedure can be outlined as follows:

1. At the initiation of the problem, or if the reference Delaunay graph has been regenerated, loop over every internal point of the fluid computational mesh and

   (a) Search for the element of the graph within which the current point is contained.
   (b) Calculate and store the volume coefficients of the reference mesh point relative to the reference Delaunay graph.

DOI: 10.1002/fld

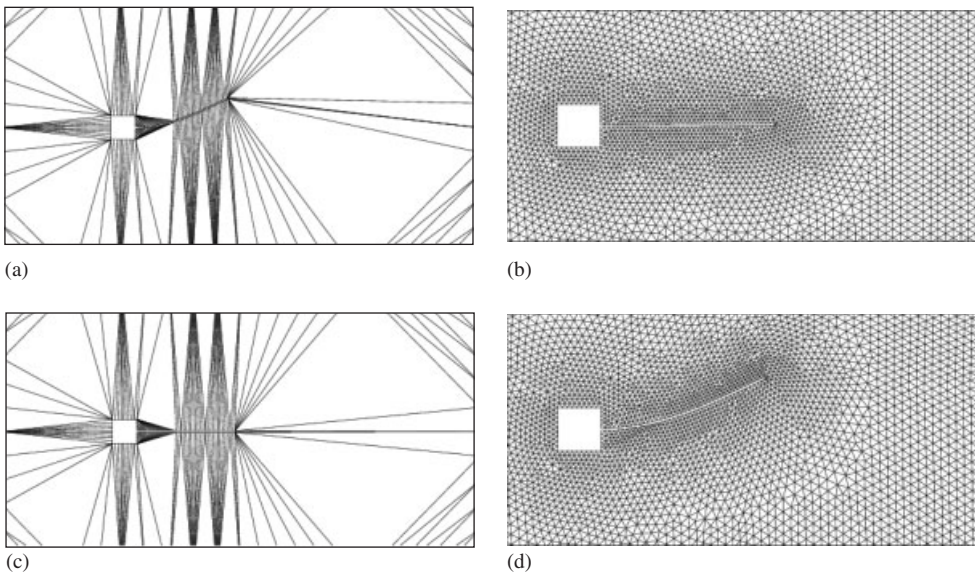

Figure 4. Mesh movement using Delaunay graph mapping: (a) the original Delaunay graph; (b) the original tetrahedral mesh; (c) the moved Delaunay graph; and (d) the moved tetrahedral mesh.

2. For every physical time step,
   (a) Apply the Dirichlet boundary conditions defined by the structural solution directly to the interface nodes of the Delaunay graph to generate the moved Delaunay graph, as shown in Figure 4(c).
   (b) Looping over all the points in the mesh, calculate the mapping of the original fluid mesh points onto the deformed Delaunay graph according to Equation (51).
   (c) Output the mesh information file with the updated coordinates as shown in Figure 4(d).

The position of the mesh point P lying within the graph tetrahedra with points $ABCD$ is uniquely defined by the four relative volume coefficients, denoted by e_i. The four tetrahedral sub-volumes V_1, V_2, V_3, V_4, the total volume V and the corresponding relative volume coefficients $e_i = V_i/V$ are calculated from the coordinates of the reference Delaunay graph points $ABCD$ and the point P. Looping over of all the points in the mesh, the moved point coordinates (x'_P, y'_P, z'_P) can then be calculated by mapping the original fluid mesh coordinates onto the deformed Delaunay graph as follows:

$$x'_P = \sum_{i=1}^{4} e_i x'_i, \quad y'_P = \sum_{i=1}^{4} e_i y'_i, \quad z'_P = \sum_{i=1}^{4} e_i z'_i \tag{51}$$

The method utilizes an Alternating Digital Tree [44] search algorithm to efficiently locate the mesh point within the Delaunay graph and is computationally inexpensive as the one-to-one mapping is calculated only at the initiation or regeneration stages of the procedure. The method ensures that primary mesh topology is maintained throughout the simulation and, unlike computationally expensive iterative methods such as the spring analogy, extreme displacements can be applied at the boundaries in a single step. This is because the movement of the boundary of the Delaunay

DOI: 10.1002/fld

graph is not restricted by issues of mesh entanglement or negative volumes that affect standard mesh movement procedures. Although the algorithm cannot proceed directly if the prescribed boundary movement renders the Delaunay triangulation invalid, this can be remedied by updating the reference Delaunay graph to the most recent deformed configuration and recalculating the one-to-one mapping between the meshes at that point.

5. NUMERICAL EXAMPLES

5.1. Flow-induced oscillations of a flexible cantilever

This two-dimensional problem has been reported extensively in the literature. Numerous authors, such as Wall [9], Hübner *et al.* [11], Matthies and Steindorf [8] and Dettmer and Perić [6], have assessed the quality of their numerical solution strategies for FSI by referring to this benchmark physical problem. A two-dimensional mesh of triangles is extruded over the third dimension to generate layers of tetrahedral elements. By employing appropriate symmetrical boundary conditions, the three-dimensional strategy presented in this paper can be applied to generate an accurate representation of the two-dimensional results reported for this problem.

A thin, elastic cantilever structure is situated in the wake of a rigid square solid body. For flows with a Reynolds number beyond a certain value, the flow past the square bluff body generates vortices, which separate from the leading corners of the rigid body with a stable frequency. This is the well-known von Kármán vortex shedding. This oscillatory behaviour of the fluid results in time-dependent lift forces, which excite the flexible beam and lead to a long-term oscillatory motion of the structure, which is dependent upon the coupled FSI. The geometry and boundary conditions of the domain are depicted in Figure 5. The material parameters of the fluid and structure

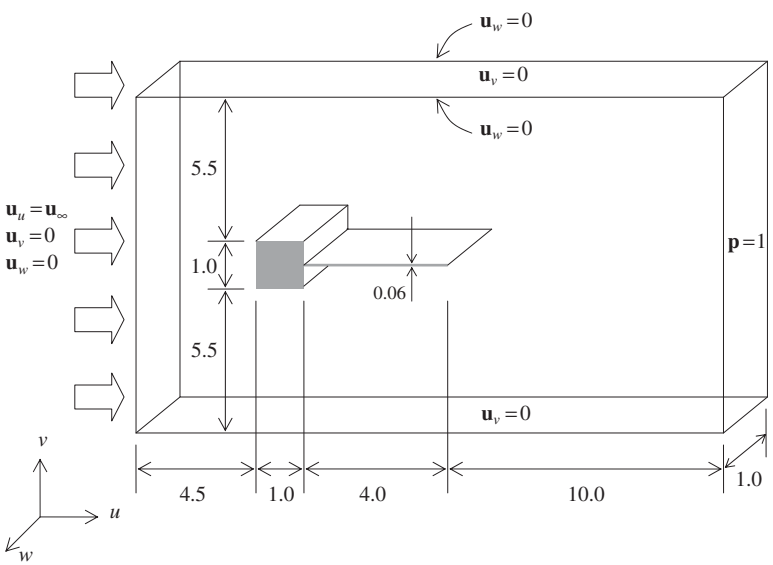

Figure 5. Geometry and boundary conditions.

DOI: 10.1002/fld

are as follows: $\mu_F = 1.82 \times 10^{-4}\,\mathrm{g/cm\,s}$, $\rho_F = 1.18 \times 10^{-3}\,\mathrm{g/cm^3}$, $\mu_S = 9.2593 \times 10^5\,\mathrm{g/cm\,s^2}$, $\rho_S = 0.1\,\mathrm{g/cm^3}$ and Poisson's ratio $v = 0.35$. The fluid inflow velocity $u_\infty = 51.3\,\mathrm{cm/s}$; thus, the Reynolds number $Re = \rho_F L u_\infty / \mu_F = 333$, where the length scale $L = 1\,\mathrm{cm}$ corresponds to the length of the side of the rigid square body. Two different finite volume–finite element representations of the system are considered to prove the mesh independence of the scheme. Firstly, the three-dimensional extruded fluid domain mesh is composed of 90 783 tetrahedra (23 334 nodes), while the structure is modelled in two dimensions using a Neo–Hookean plane stress material with a discretization of 120 9-noded Laplace elements (567 nodes) with an aspect ratio of 0.1:0.02 and quadratic shape functions to avoid artificial stiffening of the system. Similarly, in the second set of meshes the fluid domain mesh is composed of 181 368 tetrahedra (46 164 nodes) while the structure is discretized with 160 9-noded Laplace elements (805 nodes) with an aspect ratio of 0.05:0.03. To compare the results of these simulations with those reported in the literature, the analysis is performed for time steps of 0.005, 0.0075 and 0.01 s. To assess the performance of the partitioned coupling procedure, the convergence of the scheme is presented for analyses with a fixed number of subiterations.

In this benchmark example, it is found that a single subiteration per time step provides insufficient coupling at the interface. This leads to an unstable high-frequency oscillation of the structure. However, two subiterations per time step achieves sufficient coupling at the interface for a stable oscillatory motion of the structure to be achieved, as shown in Figure 6. The addition of further subiterations enables the interface coupling conditions to be enforced even more accurately with convergence typically reaching 1×10^{-4}, as shown in Figure 7. In Figure 8, the unsteady nature of the vortex shedding can be clearly distinguished. The evolution of the pressure contours and the x-component of the velocity are displayed at various points of the beam oscillation. The efficacy of the Newmark/Newton–Raphson solution algorithm of the structural solver, which iterates upon the change in acceleration, is demonstrated in Figure 9, where a smooth, undamped solution in time across acceleration, velocity and displacement is clearly achieved. The long-term coupled beam tip displacement is found to be in the range $|d_{\max}| \in [1.10, 1.20]\,\mathrm{cm}$ with an average period of oscillation in the range $T \in [0.32, 0.36]\,\mathrm{s}$. These results compare very well with those documented in the literature, which are summarized in Table I. The scheme is also verified for differing discretizations, as shown in Figure 10, and for a range of time steps, as shown in Figure 11. These results all converge to the same long-term oscillatory motion of the beam.

To assess the computational cost of the subiterative scheme, a summary of typical wall-clock timings per subiteration and the corresponding convergence values for 10 subiterations are shown

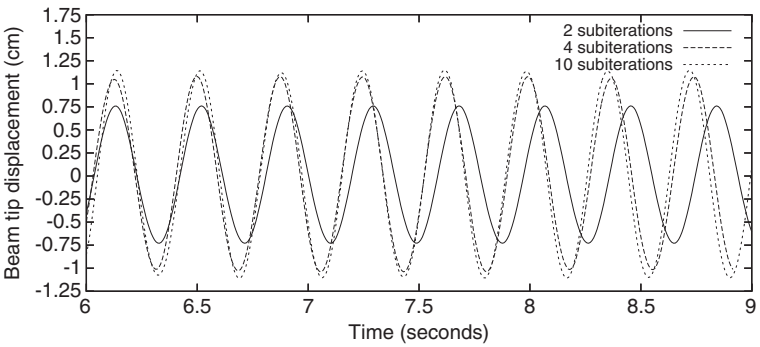

Figure 6. Beam tip displacement for 2, 4 and 10 subiterations.

DOI: 10.1002/fld

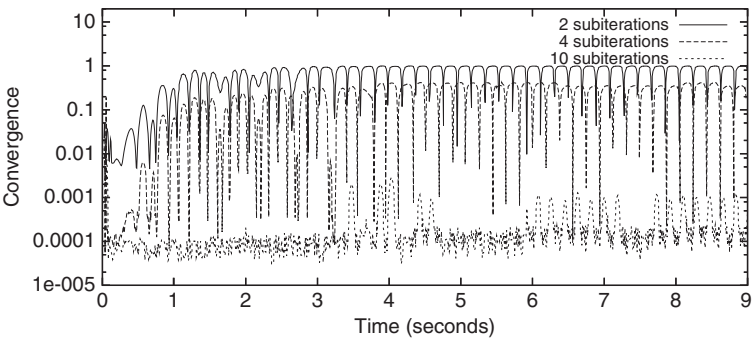

Figure 7. Convergence for 2, 4 and 10 subiterative cycles.

in Table II and displayed graphically in Figure 12. These timings are for computations on a Dell PowerEdge SC1420 Server with two Intel Xeon processors and 2GB of SDRAM. It can be seen that this example has a typical wall-clock time per time step of around 4 min when 10 subiterations are consistently applied, which results in a total run time of around four days per analysis.

5.2. Blood flow through a weakened artery

This three-dimensional problem is motivated by the growing need for accurate biomedical modelling of the human body, specifically in the area of cardiovascular medicine. In particular, doctors seek to understand more fully such critical issues as the role of wall shear stresses in cardiovascular diseases [3, 4]. Other areas of research include 'virtual surgery' [3] to predict the risk and various possible approaches prior to surgical intervention. This area of research could also be highly useful in the design and use of devices such as stents and mechanical valves. To model the systolic–diastolic cycle of blood flow through the arteries, pulsatile velocity–pressure boundary conditions are applied in the fluid domain using an approximation of the Womersley formulation [45], with prescribed time-dependent inflow velocities and outflow pressures. In addition, although blood is known to be a complex, non-Newtonian fluid, it is assumed to be Newtonian in this example. The length of the artery is taken as 10 mm with a circular cross section of diameter 1 mm. To model the effect of a weakened area of arterial wall, 3 mm of the mid-length of the artery is composed of a deformable membrane material. The material parameters of the fluid and structure are taken as follows: $\mu_F = 4 \times 10^{-3}\,\mathrm{g/mm\,s}$, $\rho_F = 1.0 \times 10^{-3}\,\mathrm{g/mm^3}$, $\mu_S = 335.57 \times 10^3\,\mathrm{g/mm\,s^2}$ and Poisson's ratio $v = 0.49$. The thickness of the arterial wall, based on the information extracted from medical imaging of real patients [4], is taken as $t = 0.075$ mm. The density of the artery wall is considered to be negligible, enabling a quasi-static analysis of the structure to be performed.

Two patient cases are considered: normal blood pressure with a base (diastole) pressure of 80 mmHg and a peak (systole) pressure of 120 mmHg, and hypertension blood pressure, with a base pressure level of 100 mmHg and a peak blood pressure of 170 mmHg. At the inflow boundary, the prescribed flow profile corresponds to the undisturbed Poiseuille flow. The peak inflow velocity is prescribed as $u_\infty = 4000$ mm/s; thus, the Reynolds number is obtained as $Re = \rho_F L u_\infty / \mu_F = 1000$, where the length scale $L = 1$ mm is the diameter of the artery. Inflow velocity and outlet pressure are assumed to vary according to the systolic/diastolic cycle in phase. The coupling procedure is performed with five subiterations per time step. The discretization of the three-dimensional fluid

DOI: 10.1002/fld

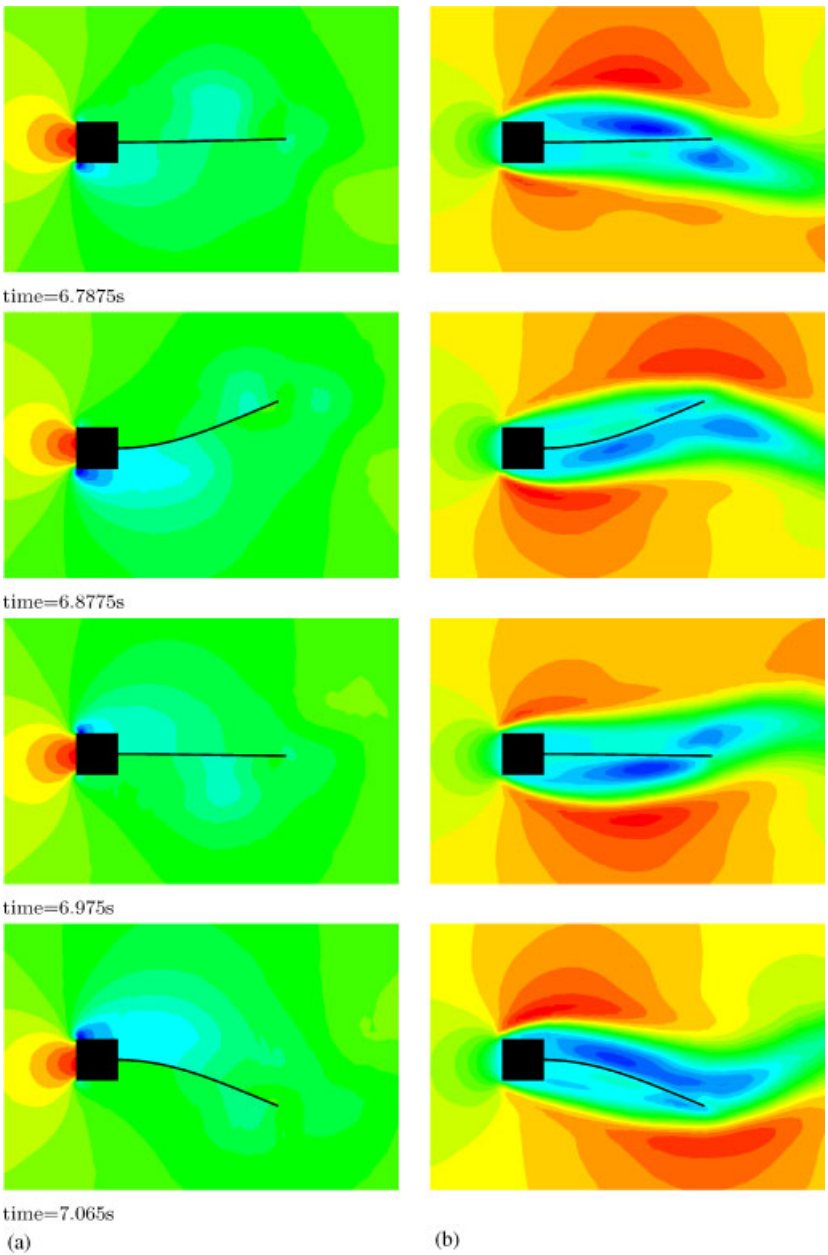

Figure 8. Oscillation of a flexible cantilever: (a) pressure and (b) x-velocity.

domain is composed of 134 400 tetrahedra (26 331 nodes). The deformable membrane component is modelled using the plane stress incompressible Neo–Hookean hyperelastic membrane material described previously, with the structure composed of 4320 3-noded triangular membrane elements (2196 nodes), see Figure 13.

DOI: 10.1002/fld

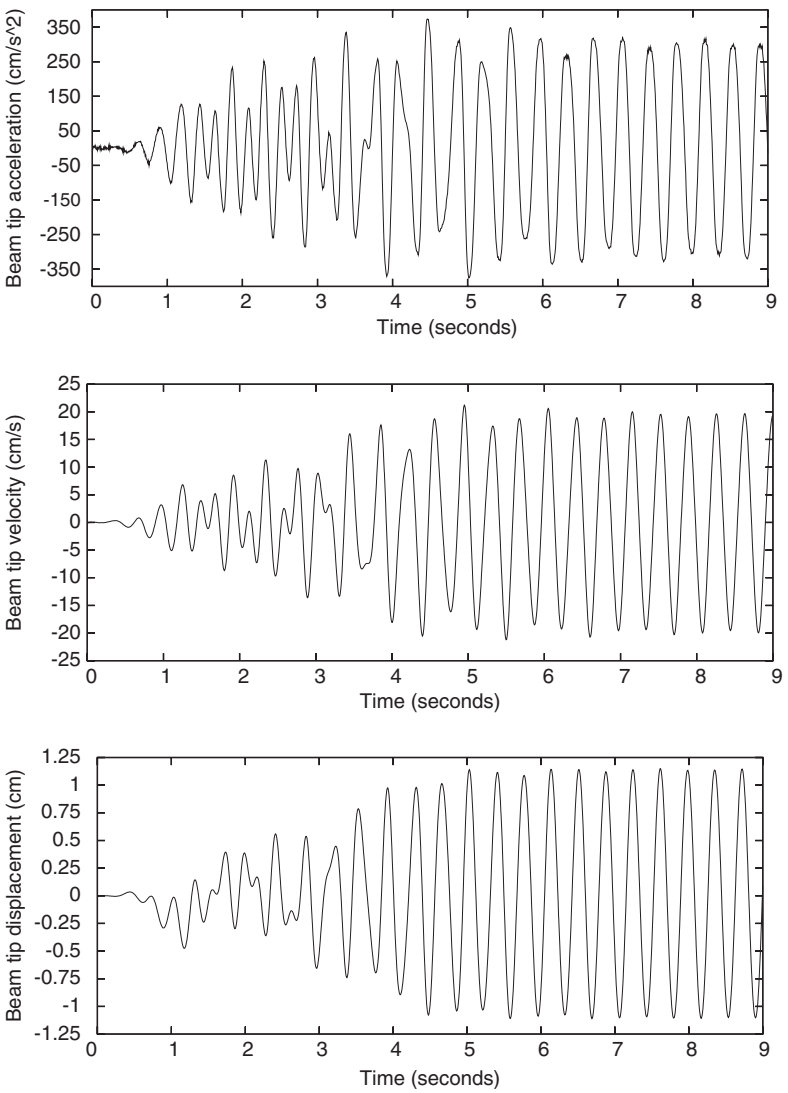

Figure 9. Beam tip acceleration, velocity and displacement.

Table I. Comparison of current results with those in the literature.

Author	Period of oscillation T (s)	Tip deflection $d_{\max}$ (cm)
Wall [9]	0.31–0.36	1.12–1.32
Matthies and Steindorf [8]	0.32	1.0–1.35
Dettmer and Perıc [6]	0.32–0.34	1.1–1.4
Current work	0.32–0.36	1.10–1.20

DOI: 10.1002/fld

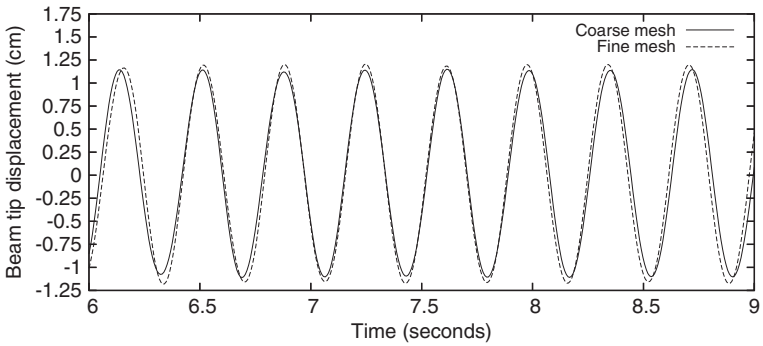

Figure 10. Beam tip displacement: comparison for coarse and fine discretizations.

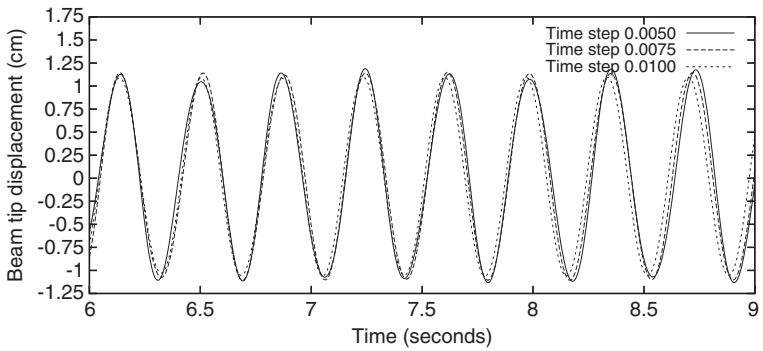

Figure 11. Beam tip displacement: comparison for $\Delta t = 0.005, 0.0075, 0.01$.

Table II. Convergence and wall-clock timings.

Subiteration	Convergence	Timing (s)
1	1.00	105
2	1.34×10^{-2}	50
3	3.13×10^{-3}	23
4	3.30×10^{-4}	14
5	1.84×10^{-5}	12
6	9.35×10^{-6}	12
7	7.83×10^{-6}	12
8	7.78×10^{-6}	12
9	6.76×10^{-6}	12
10	5.75×10^{-6}	12

DOI: 10.1002/fld

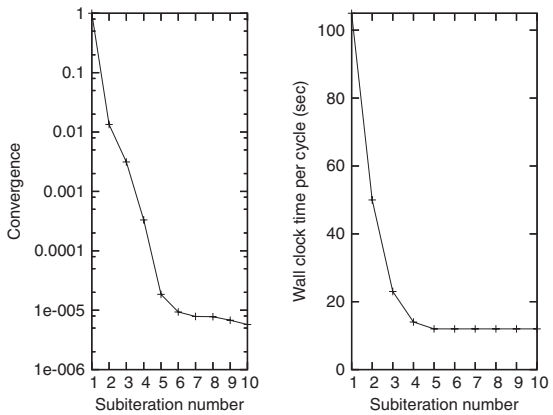

Figure 12. Performance over 10 subiterations.

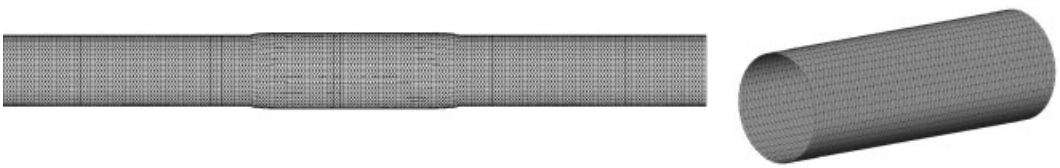

Figure 13. Discretization of the fluid and structure domains.

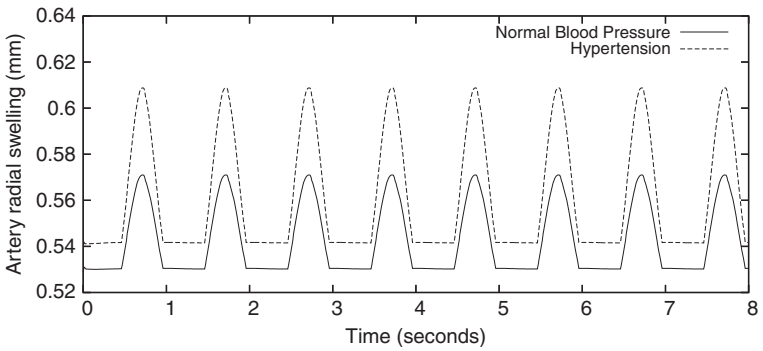

Figure 14. Normal and hypertensive blood pressure: wall movement.

Figure 15 shows the evolution of the aneurysm wall movement in time over several systolic/diastolic cycles. Analysis of these results shows that in the case of normal blood pressure, the base flow causes the aneurysm to swell by 3.0×10^{-2} mm (6% of the radius) and at peak flow this increases to 7.0×10^{-2} mm (14% of the radius). In the hypertension case, the base flow causes the aneurysm to swell radially by 4.0×10^{-2} mm (8% of the radius) and at peak flow this increases to 11.0×10^{-2} mm (22% of the radius). Cuts through the domain, as shown in Figures 16 and 17, reveal the fluid pressure and velocity profiles within the aneurysm. It can be observed

DOI: 10.1002/fld

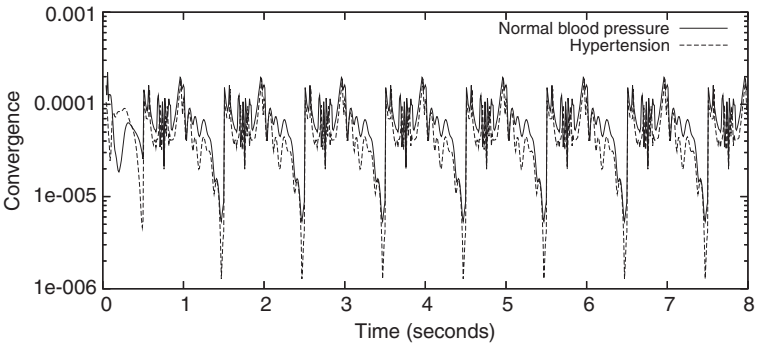

Figure 15. Normal and hypertensive blood pressure: convergence.

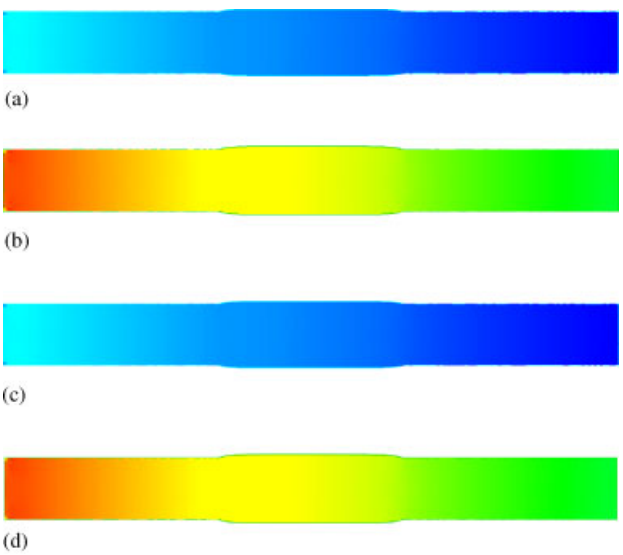

Figure 16. Fluid pressure. Normal BP: (a) diastole and (b) systole. Hypertension BP: (c) diastole and (d) systole.

that the fluid velocity is greatly reduced in the area of the aneurysm. Comparison of the results of the structural analyses for the normal and hypertensive pressure cases, as shown in Figures 18 and 19, reveal considerable differences in the membrane structural response for the two patient cases, with maximum principal stretches of 1.23 in the hypertensive case and the corresponding principal stresses nearly double that of the normal blood pressure case. These results are found to be consistent over a range of time steps, with values of radial expansion due to the blood pressure variations in each case comparing well with those in the literature [4]. The convergence history of the scheme, as shown in Figure 14, indicates that the coupling procedure consistently reaches a level of convergence below 1×10^{-4}, with a typical wall-clock time per time step of around 7 min when five subiterations are consistently applied.

DOI: 10.1002/fld

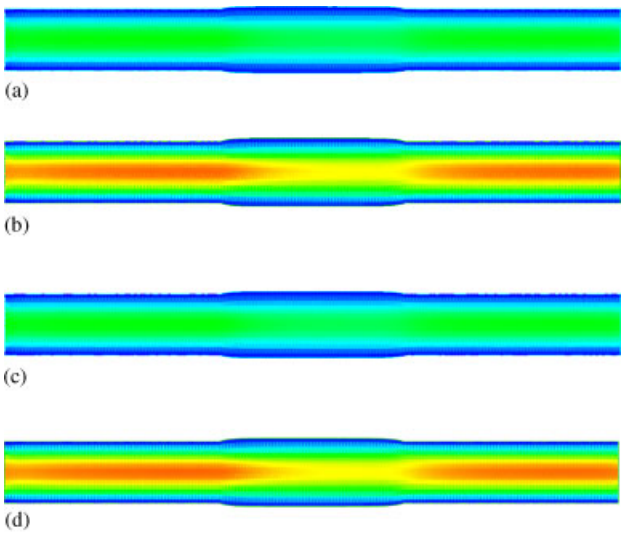

Figure 17. Fluid x-velocity. Normal BP: (a) diastole and (b) systole. Hypertension BP: (c) diastole and (d) systole.

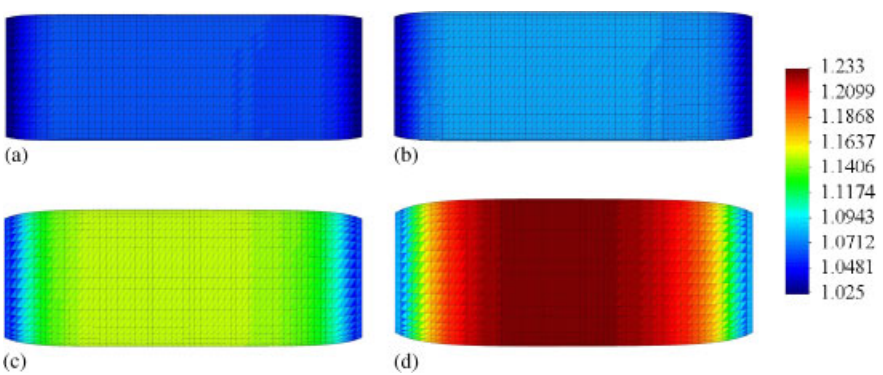

Figure 18. Maximum principal stretches over the aneurysm. Normal BP: (a) diastole and (c) systole. Hypertension BP: (b) diastole and (d) systole.

6. CONCLUSIONS

A computational partitioned coupling strategy for the modelling of large deformation FSI has been presented, enabling a modular approach to be adopted for the fluid, structure and moving interface subproblems. The accuracy of the algorithm is demonstrated with respect to reported results in the literature for a benchmark example. The algorithm proven to be robust over a range of time steps and discretizations and the computational efficiency of the subiterative coupling scheme have also been assessed. The three-dimensional unsteady incompressible fluid is solved using a powerful implicit dual time-stepping technique with explicit multistage Runga–Kutta pseudo-time

DOI: 10.1002/fld

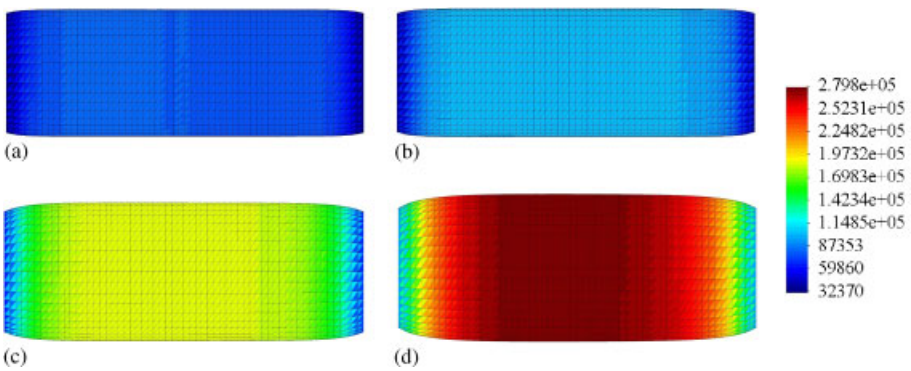

Figure 19. Maximum principal stresses over the aneurysm. Normal BP: (a) diastole and (c) systole. Hypertension BP: (b) diastole and (d) systole.

stepping and an ALE formulation for the moving boundaries, and it should be noted that this coupling strategy would enable the fluid model to be extended to compressible and turbulent flow regimes. The large deformation three-dimensional dynamic structure is solved using a finite strain continuum approach with a quadratically convergent Newton–Raphson iterative scheme. Mesh movement in three dimensions utilizes a Delaunay graph mapping procedure, which has been found to be highly effective even for large boundary movements within the fluid domain. The coupling strategy ensures compatibility of the displacement and velocity boundary conditions at the interface at each time step, with corrective subiteration to ensure convergence of the interface pressure field. This partitioned strategy seems ideally suited to the modelling of FSI problems even for very flexible structures and further work on a coupling strategy with improved efficiency is currently in preparation.

ACKNOWLEDGEMENTS

C. Wood gratefully acknowledges the Research Studentship provided by the U.K. Engineering and Physical Sciences Research Council (EPSRC). O. Hassan acknowledges the support provided by the EPSRC through Platform Grant EP/D074258.

REFERENCES

1. De Hart J, Peters GW, Schreurs PJ, Baaijens FP. A three-dimensional computational analysis of fluid–structure interaction in the aortic valve. *Journal of Biomechanics* 2003; **36**(1):103–112.
2. Liu WK, Liu Y, Farrell D, Zhang L, Wang XS, Fukui Y, Patankar N, Zhang Y, Bajaj C, Lee J, Hong J, Chen X, Hsu H. Immersed finite element method and its applications to biological systems. *Computer Methods in Applied Mechanics and Engineering* 2006; **195**:1722–1749.
3. Taylor CA, Hughes TJR, Zarins CK. Computational investigations in vascular disease. *Computational Physics* 1996; **10**(3):224–232.
4. Torii R, Oshima M, Kobayashi T, Takagi K, Tezduyar T. Fluid–structure interaction modelling of aneurysmal conditions with high and normal blood pressures. *Computational Mechanics* 2006; **38**:482–490.
5. Peskin CS. Flow patterns around heart valves: a numerical method. *Journal of Computational Physics* 1972; **10**:252–271.
6. Dettmer W, Perić D. A computational framework for fluid–structure interaction: finite element formulation and applications. *Computer Methods in Applied Mechanics and Engineering* 2006; **195**:5754–5779.

DOI: 10.1002/fld

7. Farhat C, Lesoinne M, Maman N. Mixed explicit/implicit time integration of coupled aeroelastic problems: three-field formulation, geometric conservation and distributed solution. *International Journal for Numerical Methods in Fluids* 1995; **21**:807–835.
8. Matthies HG, Steindorf J. Partitioned strong coupling algorithms for fluid–structure interaction. *Computers and Structures* 2003; **81**:805–812.
9. Wall WA. Fluid–struktur-interaktion mitstabilisieten finiten elementen. *Ph.D. Thesis*, Universität Stuttgart, Institut für Baustatik, 2000.
10. Hansbo P. The characteristic streamline diffusion method for the time-dependent incompressible Navier–Stokes equations. *Computer Methods in Applied Mechanics and Engineering* 1992; **99**:171–186.
11. Hübner B, Walhorn E, Dinkler D. A monolithic approach to fluid–structure interaction using space–time finite elements. *Computer Methods in Applied Mechanics and Engineering* 2004; **193**:2087–2104.
12. Hughes TJR, Hulbert GM. Space–time finite element methods for elastodynamics: formulations and error estimates. *Computer Methods in Applied Mechanics and Engineering* 1988; **66**:339–363.
13. Stein KR, Benney R, Tezduyar T, Potvin J. Fluid–structure interactions of a cross parachute: numerical simulation. *Computer Methods in Applied Mechanics and Engineering* 2001; **191**:673–687.
14. Tezduyar TE, Behr M, Liou J. A new strategy for finite element computations involving moving boundaries and interfaces—the deforming-spatial-domain/space–time procedure: I. The concept and preliminary numerical tests. *Computer Methods in Applied Mechanics and Engineering* 1992; **94**:339–351.
15. Donea J, Jiuliani S. Halleux JP. An arbitrary Lagrangian–Eulerian finite element method for transient dynamic fluid–structure interactions. *Computer Methods in Applied Mechanics and Engineering* 1982; **33**:689–723.
16. Hughes TJR, Liu WK, Zimmerman T. An arbitrary Lagrangian–Eulerian finite element formulation for incompressible viscous flow. *Computer Methods in Applied Mechanics and Engineering* 1981; **29**:329–349.
17. Belytschko T, Liu WK, Moran B. *Nonlinear Finite Elements for Continua and Structures*. Wiley: New York, 2000.
18. Bonet J, Wood RD. *Non-linear Continuum Mechanics for Finite Element Analysis*. Cambridge University Press: Cambridge, 1997.
19. Batina JT. Unsteady Euler airfoil solutions using unstructured dynamic meshes. *Twenty-seventh AIAA Aerospace Sciences Meeting* (*AIAA-1989-115*), Reno, NV, U.S.A., 1989.
20. Degand C, Farhat C. A three-dimensional torsional spring analogy method for unstructured dynamic meshes. *Computers and Structures* 2002; **80**:305–316.
21. Liu X, Qin N, Xia H. Fast dynamic grid deformation based on Delaunay graph mapping. *Journal of Computational Physics* 2006; **211**:405–423.
22. Blom FJ. A monolithical fluid–structure interaction algorithm applied to the piston problem. *Computer Methods in Applied Mechanics and Engineering* 1998; **167**:369–391.
23. Bletzinger KU, Gallinger T, Kupzok A, Wuchner R. Partitioned strategies for optimization on FSI. *Proceedings of the European Conference on Computational Fluid Dynamics*, Delft, 2006.
24. Chorin AJ. A numerical method for solving incompressible viscous flow problems. *Journal of Computational Physics* 1967; **2**:12–26.
25. Turkel E. Preconditioned methods for solving the incompressible and low speed compressible equations. *Journal of Computational Physics* 1987; **72**:277–298.
26. Rizzi A, Eriksson LE. Computation of inviscid incompressible flow with rotation. *Journal of Fluid Mechanics* 1985; **153**:275–312.
27. Gil AJ, Zhang Z, Hassan O, Morgan K. A parallel unsteady multigrid DES algorithm for the solution of 3D incompressible flows on unstructured grids. *Journal of Aerospace Engineering* 2006; **19**:271–280.
28. Hassan O, Sørensen K, Morgan K, Weatherill NP. A method for time accurate turbulent compressible fluid flow simulation with moving boundary components employing local remeshing. *International Journal for Numerical Methods in Fluids* 2007; **53**:1243–1266.
29. Sørensen KA. A multigrid accelerated procedure for the solution of compressible fluid flows on unstructured hybrid meshes. *Ph.D. Thesis*, University of Wales, Swansea, 2001.
30. Zhang Z, Gil AJ, Hassan O, Morgan K. The simulation of 3D unsteady incompressible flows with moving boundaries on unstructured meshes. *Computers and Fluids* 2007; DOI: 10.1016/j.compfluid.2007.07.013.
31. Thomas PD, Lombard CK. Geometric conservation law and its application to flow computations on moving grids. *AIAA Journal* 1979; **17**:1030–1037.
32. Farhat C, Geuzaine P, Grandmont C. The discrete geometric conservation law and the nonlinear stability of ALE schemes for the solution of flow problems on moving grids. *Journal of Computational Physics* 2001; **174**:669–694.

DOI: 10.1002/fld

33. Koobus B, Farhat C. Second-order time-accurate and geometrically conservative implicit schemes for flow computations on unstructured dynamic meshes. *Computer Methods in Applied Mechanics and Engineering* 1999; **170**:103–129.
34. Lesoinne M, Farhat C, Maman N. Geometric conservation laws for problems involving moving boundaries and deforming meshes, and their impact on aeroelastic computations. *Computer Methods in Applied Mechanics and Engineering* 1996; **134**:71–90.
35. Nkonga B, Guillard H. Godunov type method on non-structured meshes for three-dimensional moving boundary problems. *Computer Methods in Applied Mechanics and Engineering* 1994; **113**:183–204.
36. Venkatakrishnan V, Mavriplis DJ. Implicit method for the computation of unsteady flows on unstructured grids. *Journal of Computational Physics* 1996; **127**:380–397.
37. Jameson A, Schmidt W, Turkel E. Numerical simulation of the Euler equations by finite volume methods using Runge–Kutta timestepping schemes. *AIAA Aerospace Sciences Meeting* (*AIAA-1981-1259*), Reno, NV, U.S.A., 1981.
38. Holzapfel GA, Eberlein R, Wriggers P, Weizsäcker HW. Large strain analysis of soft biological membranes: formulation and finite element analysis. *Computer Methods in Applied Mechanics and Engineering* 1996; **132**: 45–61.
39. Bathe KJ. *Finite Element Procedures*. Prentice-Hall: Englewood Cliffs, NJ, 1996.
40. Hughes TJR. *The Finite Element Method*. Dover: New York, 2000.
41. Causin P, Gerbeau JF, Nobile F. Added-mass effect in the design of partitioned algorithms for fluid–structure problems. *Computer Methods in Applied Mechanics and Engineering* 2005; **194**:4506–4527.
42. Förster C, Wall WA, Ramm E. Artificial added mass instabilities in sequential staggered coupling of nonlinear structures and incompressible viscous flows. *Computer Methods in Applied Mechanics and Engineering* 2007; **196**:1278–1293.
43. Weatherill NP, Hassan O. Efficient three-dimensional Delaunay triangulation with automatic boundary point creation and imposed boundary constraints. *International Journal for Numerical Methods in Engineering* 1994; **37**:2005–2039.
44. Bonet J, Peraire J. An alternating digital tree (ADT) algorithm for 3D geometric searching and intersection problems. *International Journal for Numerical Methods in Engineering* 1991; **31**(1):1–17.
45. Womersley JR. Method for the calculation of velocity, rate of flow and viscous drag in arteries when the pressure gradient is known. *Journal of Physiology* 1955; **127**:553–563.

DOI: 10.1002/fld